

A Bayesian inference of relativistic mean-field model for neutron star matter from observation of NICER and GW170817/AT2017gfo

ZHENYU ZHU,¹ ANG LI,² AND TONG LIU²

¹*Tsung-Dao Lee Institute, Shanghai Jiao Tong University, Shanghai 201210, China; zhenyu.zhu@sjtu.edu.cn*

²*Department of Astronomy, Xiamen University, Xiamen, Fujian 361005, China; liang@xmu.edu.cn; tongliu@xmu.edu.cn*

(Dated: November 4, 2022)

ABSTRACT

The observations of optical and near-infrared counterparts of binary neutron star mergers not only enrich our knowledge about the abundance of heavy elements in the Universe, or help reveal the remnant object just after the merger as generally known, but also can effectively constrain dense nuclear matter properties and the equation of state (EOS) in the interior of the merging stars. Following the relativistic mean-field description of nuclear matter, we perform the Bayesian inference of the EOS and the nuclear matter properties using the first multi-messenger event GW170817/AT2017gfo, together with the NICER mass-radius measurements of pulsars. The kilonova is described by a radiation-transfer model with the dynamical ejecta, and light curves connect with the EOS through the quasi-universal relations between the ejecta properties (the ejected mass, velocity, opacity or electron fraction) and binary parameters (the mass ratio and reduced tidal deformability). It is found that the posterior distributions of the reduced tidal deformability from the AT2017gfo analysis display a bimodal structure, with the first peak enhanced by the GW170817 data, leading to slightly softened posterior EOSs, while the second peak cannot be achieved by a nuclear EOS with saturation properties in their empirical ranges. The inclusion of NICER data in our analyses results in stiffened EOS posterior because of the massive pulsar PSR J0740+6620. We give results at nuclear saturation density for the nuclear incompressibility, the symmetry energy and its slope, as well as the nucleon effective mass, from our analysis of those observational data.

Keywords: Neutron stars (1108); Gravitational waves (678); Pulsars (1306)

1. INTRODUCTION

The detection of gravitational waves (GWs) and light from the binary neutron star merger GW170817 marked the first milestone of multimessenger astronomy (Abbott et al. 2017). The GW signals from coalescing binary neutron stars have been widely used to provide critical insights into the nature of dense nuclear matter and the equation of state (EOS; i.e., the pressure-density relation) of neutron stars (Abbott et al. 2018). The electromagnetic counterparts of GW sources provide another way of studying the EOS. In particular, the transient optical/infrared/UV event (AT2017gfo) was detected several hours after the merger time of GW170817 (Andreoni et al. 2017; Arcavi et al. 2017; Coulter et al. 2017; Cowperthwaite et al. 2017; Díaz et al. 2017; Drout et al. 2017; Evans et al. 2017; Hu et al. 2017; Kasliwal et al. 2017; Lipunov et al. 2017; Pian et al. 2017; Pozanenko et al. 2018; Shappee et al. 2017; Smartt et al. 2017; Tanvir et al. 2017; Troja et al. 2017; Utsumi et al. 2017; Valenti

et al. 2017), the luminosity, spectrum and light curve of which are consistent with the prediction of the kilonova model, which attribute its emission to the *r*-process nucleosynthesis of the ejected neutron-rich matter from the merger. The mass, velocity and electron fraction of the ejecta are key parameters for understanding the observations of AT2017gfo (e.g., Metzger 2017; Perego et al. 2017; Yu et al. 2018; Ren et al. 2019; Qi et al. 2022), and closely related to the binary parameters (like the mass ratio, the radius) and the EOS (e.g., Shibata & Hotokezaka 2019).

Stiffness or softness of the EOS implies larger or smaller stellar radius and orbital separation at merger. A softer EOS and smaller radius results in a more violent collision and more efficient shock heating, which can eject more material with higher velocity and high temperature. The ejected matter with high temperature may trigger the weak interaction and neutrino emission, and further vary the electron fraction of ejecta. There-

fore, the EOS affects the input quantities of the kilonova light curve model, and it is interesting and important to infer the EOS from both the GW and kilonova data.

Merger simulations have revealed some quasi-universal relations of ejecta properties and binary parameters (mass ratio and reduced tidal deformability) (Nedora et al. 2021). The EOS constraints from kilonova observation have also been investigated (e.g., Margalit & Metzger 2017; Radice et al. 2018b; Coughlin et al. 2019; Breschi et al. 2021; Holmbeck et al. 2022). A group of EOSs from different nuclear many-body frameworks, or the parameterizations of EOS such as piecewise polytropes (Most et al. 2018; De et al. 2018; Ecker & Rezzolla 2022), or spectral parametrization (Lindblom 2010; Kolgiannis & Moustakidis 2019) were usually adopted, allowing the study only on the pressure-versus-density function, but not on the physical properties of nuclear matter.

In this work, we perform one of the first studies to connect nuclear matter microscopic parameters to the AT2017gfo data (Villar et al. 2017) of the GW170817 binary neutron star merger. The kilonova is described by a radiation-transfer model depending on which we reproduce important properties of AT2017gfo light curves and explore the underlying phase state of nuclear matter and the EOS. Nuclear matter and the EOS are described by the relativistic mean-field (RMF) model, which encodes a great amount of nuclear physics in a handful of model parameters. By construction, the RMF effective interactions can facilitate easy incorporation of various nuclear EOS constraints at the nuclear saturation density n_0 and moderate values of the isospin asymmetry. In combination with the GW observations of tidal deformability (Abbott et al. 2019) by LIGO/Virgo and the mass and radius measurements of PSR J0030+0451 and PSR J0740+6620 (Miller et al. 2019; Riley et al. 2019a; Miller et al. 2021; Riley et al. 2021a) by the NASA Neutron Star Interior Composition Explorer (NICER) mission, the inference will be performed directly on key properties like the nuclear incompressibility and the symmetry energy as well as the single particle nucleon effective mass in medium, that can be confronted with laboratory studies on nuclear structure and reactions. We do not consider the nonnucleon degree of freedom possibly present in heavy neutron stars since the data we utilize here are mostly from typical stars around or below $1.4 M_\odot$ and our main interest of the present study is the EOS parameters around the saturation density n_0 . Because the stellar radius is controlled mainly by the density dependence of the nuclear symmetry energy around n_0 (Lattimer & Prakash 2000), below we report also the most preferred radius and tidal deformability (scaling

as the fifth power of the radius) for typical $1.4 M_\odot$ stars based on our analysis. See e.g., Miao et al. (2020); Li et al. (2021a,b); Sun et al. (2022); Miao et al. (2022a,b) for analysis incorporating strangeness phase transitions in neutron star matter.

The paper is organized as follows. In Sec. 2, we will introduce the models of EOS and kilonova that employed in our analyses. In Sec. 3, we recall the Bayesian formulation and describe the parameters, priors and likelihood functions in our analyses. In Sec. 4, we present our results and discussions. Finally, we conclude in Sec. 5.

2. MODELS OF NEUTRON STAR EOS AND KILONOVA

In this section, we will review the adopted models of neutron star EOS and kilonova, including a detailed description of the relations between the kilonova observations and the EOS as well as the stellar properties.

2.1. neutron star EOS

The only physics that spherically-symmetric neutron stars in hydrostatic equilibrium are sensitive to is the EOS of (neutron-rich) nuclear matter, in the simple case of no strangeness phase transition (Li et al. 2020). In principle, it can be determined by the strong interaction, from solving the first principle QCD. Nevertheless, the complexity of nonperturbative strong interaction makes it difficult to do theoretically, and hence parameterization are widely used to describe the EOS in the analyses of observational data. Presently, the RMF nuclear many-body model is employed in our analyses.

The RMF model starts from a many-body Lagrangian for describing the nucleon-nucleon interactions, which are mediated by scalar (σ), isoscalar-vector (ω) and isovector-vector (ρ) mesons (see e.g., Li et al. 2008; Zhu et al. 2018, 2019),

$$\begin{aligned} \mathcal{L} = & \bar{\psi} (i\gamma_\mu \partial^\mu - M_N + g_\sigma \sigma - g_\omega \omega \gamma^0 - g_\rho \rho \tau_3 \gamma^0) \psi \\ & - \frac{1}{2}(\nabla \sigma)^2 - \frac{1}{2}m_\sigma^2 \sigma^2 - \frac{1}{3}g_2 \sigma^3 - \frac{1}{4}g_3 \sigma^4 \\ & + \frac{1}{2}(\nabla \omega)^2 + \frac{1}{2}m_\omega^2 \omega^2 + \frac{1}{2}g_\omega^2 \omega^2 \Lambda_v g_\rho^2 \rho^2 \\ & + \frac{1}{2}(\nabla \rho)^2 + \frac{1}{2}m_\rho^2 \rho^2, \end{aligned} \quad (1)$$

where g_σ , g_ω and g_ρ are the nucleon coupling constants for σ , ω and ρ mesons. We also include the nonlinear σ self-interactions with two parameters g_2 and g_3 , and the ω - ρ coupling with parameter Λ_v . These six meson coupling parameters can be obtained by fitting the empirical data at the nuclear saturation density n_0 (see below in Table 1).

The equation of motion for each meson can be generated by the Euler-Lagrangian equation from the La-

grangian and applying the mean-field approximation:

$$m_\sigma^2 \sigma + g_2 \sigma^2 + g_3 \sigma^3 = g_\sigma n_s, \quad (2)$$

$$(m_\omega^2 + \Lambda_v g_\omega^2 g_\rho^2 \rho^2) \omega = g_\omega (n_p + n_n), \quad (3)$$

$$(m_\rho^2 + \Lambda_v g_\omega^2 g_\rho^2 \omega^2) \rho = g_\rho (n_p - n_n). \quad (4)$$

where

$$n_s = \sum_{i=n,p} \frac{1}{\pi^2} \int_0^{p_F} \frac{M_N^*}{\sqrt{M_N^{*2} + p_F^2}} p_F^2 dp_F \quad (5)$$

is the scalar density, the p_F denotes the fermi momentum, and $M_N^* = M_N - g_\sigma \sigma$ is the effective mass. The number density of proton and neutron are represented by n_p and n_n , respectively. After solving these equations of motion, the energy density and pressure of nuclear matter can be computed by:

$$e = \sum_{i=n,p} e_{\text{kin}}^i + \frac{1}{2} m_\sigma^2 \sigma^2 + \frac{1}{3} g_2 \sigma^3 + \frac{1}{4} g_3 \sigma^4 - \frac{1}{2} m_\omega^2 \omega^2 - \frac{1}{2} m_\rho^2 \rho^2 - \frac{1}{2} \Lambda_v (g_\omega g_\rho \omega \rho)^2 + g_\omega \omega (n_n + n_p) + g_\rho \rho (n_p - n_n), \quad (6)$$

$$p = \sum_{i=n,p} p_{\text{kin}}^i - \frac{1}{2} m_\sigma^2 \sigma^2 - \frac{1}{3} g_2 \sigma^3 - \frac{1}{4} g_3 \sigma^4 + \frac{1}{2} m_\omega^2 \omega^2 + \frac{1}{2} m_\rho^2 \rho^2 + \frac{1}{2} \Lambda_v (g_\omega g_\rho \omega \rho)^2. \quad (7)$$

To study the structure of neutron stars, we have to calculate the composition and EOS of cold, neutrino-free, catalyzed matter. We require that the neutron star contains charge-neutral matter consisting of neutrons, protons, and leptons (e^- , μ^-) in beta equilibrium. Additionally, since we are looking at neutron stars after neutrinos have escaped, we set the neutrino chemical potentials equal to zero. Also, we use ultrarelativistic and nonrelativistic approximations for the electrons and muons, respectively, and their contributions to the energy and pressure are merely added to the Eqs. (6)–(7). Consequently, the energy density and pressure of neutron star matter are simply the functions of nucleon number density.

For completeness, we also write down the expressions of the symmetry energy J_0 , incompressibility K_0 and symmetry energy slope L_0 at the saturation density in

symmetric nuclear matter

$$J_0 = \frac{p_F^2}{6E_F} + \frac{g_\rho^2}{2[m_\rho^2 + \Lambda_v (g_\omega g_\rho \omega)^2]} (n_p + n_n), \quad (8)$$

$$K_0 = \frac{3p_F^2}{E_F} + \frac{3M_N^* p_F}{E_F} \frac{dM_N^*}{dp_F} + \frac{9g_\omega^2}{m_\omega^2 + \Lambda_v (g_\omega g_\rho \rho)^2} n_0, \quad (9)$$

$$L_0 = 3J_0 + \frac{1}{2} \left(\frac{3\pi^2}{2} n_0 \right)^{2/3} \frac{1}{E_F} \times \left(\frac{g_\omega^2}{m_\omega^2 + \Lambda_v (g_\omega g_\rho \rho)^2} \frac{n_0}{E_F} - \frac{K_0}{9E_F} - \frac{1}{3} \right) - \left(\frac{3g_\rho^2}{m_\rho^2 + \Lambda_v (g_\omega g_\rho \omega)^2} \right)^2 \frac{g_\omega^3 \Lambda_v \omega n_0^2}{m_\omega^2 + \Lambda_v (g_\omega g_\rho \rho)^2}. \quad (10)$$

To recap, we have six nuclear matter properties: The saturation density n_0 , energy per baryon E/A , J_0 , K_0 , L_0 and effective mass M_N^* , to be reproduced to fitting the six model parameters, g_σ , g_ω , g_ρ , g_2 , g_3 and Λ_v . Once the saturation properties of nuclear matter are chosen in their empirical ranges, the six model parameters can be uniquely determined (see Appendix A for more details) for the calculations of neutron stars. In our following analysis, we will directly specify these six saturation properties, rather than the model parameters, to denote the EOS.

2.2. Kilonovae

In the present work, we employed a radiation transfer model (see e.g., Metzger 2017; Yu et al. 2018; Ren et al. 2019; Qi et al. 2022, for more details) to calculate the light curves of the kilonova. The emission luminosity is computed by solving the energy conservation equations of ejecta, where the heating of r -process nucleosynthesis and the cooling of adiabatic expansion are taken into account. Additionally, the source of kilonova is treated as a blackbody and the spectra are given by the blackbody emission.

The ejecta during and after the binary neutron star merger mainly consists of two components, i.e., dynamical ejecta and wind-driven ejecta. The dynamical ejection is driven by the tidal forces during the inspiral and shock heating during the coalescence (Bovard et al. 2017; Radice et al. 2018a; Shibata & Hotokezaka 2019). The tidal forces eject the material primarily along the direction of the equator with relatively low temperature and low electron fraction (smaller than 0.1-0.2). Meanwhile, the shock isotropically ejects and heats the material to a high temperature where the weak interaction can be triggered so that the electron fraction increases. Therefore, The ejecta driven by shock heating has a high electron fraction ($Y_e > 0.25$) and distributes evenly along

the inclination θ . In addition to the dynamic ejecta, the neutrino emissions from the remnant before collapsing to black hole as well as the viscosity could further drive more ejecta (the so-called wind-driven ejecta) from the disc surrounding the remnant, which naturally more subject to e.g., the lifetime of the remnant neutron star. For the present study, we do not consider the wind-driven ejecta when connecting the AT2017gfo observational data with the underlying EOS.

The ejected matter with a low electron fraction that mainly concentrates on the orbital plane will undergo a full r -process nucleosynthesis and produce a large amount of lanthanide elements. The high opacity result from the lanthanide elements leads the ejecta on the orbital plane to be the “red” component. On the other hand, the ejected material along the polar direction is primarily contributed by the shock heating, and will only experience a partial r -process nucleosynthesis, whose lanthanide synthesis is suppressed. consequently, the polar ejecta has a relatively lower opacity and is called “blue” component.

The multi-wavelength light curves of AT2017gfo indicate that it cannot be explained by the models with only one single set of parameters, if only the power of r -process nuclei is taken into account (Villar et al. 2017). Therefore, we involved both the “red” and “blue” component in our model by implementing a θ -dependent opacity. The ejected material is approximated as being homologously expanding, and the shell structure is formed accordingly. Each shell can further be decomposed into two patches with different opacity, and the interface of these two patches is set to be $\theta = \pi/4$. Therefore, the opacity can be described by a step function of inclination angle θ :

$$\kappa = \begin{cases} \kappa_{\text{low}}, & \theta \leq \pi/4 ; \\ \kappa_{\text{high}}, & \theta > \pi/4 , \end{cases} \quad (11)$$

where opacity is denoted by κ . κ_{low} and κ_{high} are constants and correspond to the “blue” and “red” component of the kilonova.

Because of the isotropic distribution of mass, the density is merely the function of radial coordinate r . This distribution is typically described by a power-law (see Nagakura et al. 2014), and the density distribution function of radius can be written as:

$$\rho_{\text{ej}}(R) = \frac{M_{\text{ej}}}{4\pi} (3 - \delta) \frac{R^{-\delta}}{R_{\text{max}}^{3-\delta} - R_{\text{min}}^{3-\delta}} , \quad (12)$$

where the total mass, the maximal and minimal radius of the ejecta is denoted by M_{ej} , R_{max} , and R_{min} , respectively. The shell with the maximum and minimal

radius also represents the maximum and minimum velocity shell through $R_{\text{max}} = v_{\text{max}}t$ and $R_{\text{min}} = v_{\text{min}}t$. The index δ is a constant between 1 and 3. With this distribution function, the mass of each shell can be calculated by integrating over the radius.

The emission luminosity can be obtained by solving the equation of energy conservation:

$$\frac{dE_{i,j}}{dt} = m_{i,j} \dot{q}_r \eta_{\text{th}} - \frac{E_{i,j}}{R_i} \frac{dR_i}{dt} - L_{i,j} , \quad (13)$$

where i, j denotes the index of patches (indicating that the patch locates at the i th shell and j th inclination angular spacing), and $m_{i,j}$ represents the mass of the patch. Because the opacity is a step function and only two value is available in our computation, the number of patches for each shell is 2 ($j = 1, 2$). The first term on the right-hand side of this equation represents the heating of r -process nucleosynthesis. The \dot{q}_r denotes the radioactive power per unit mass and η_{th} denotes the thermalization efficiency. They can be written as (Kobrin et al. 2012; Barnes et al. 2016):

$$\dot{q}_r = 4 \times 10^{18} \left[\frac{1}{2} - \frac{1}{\pi} \arctan \left(\frac{t - t_0}{\sigma} \right) \right]^{1.3} \text{ erg s}^{-1} \text{ g}^{-1} ,$$

$$\eta_{\text{th}} = 0.36 \left[\exp(-0.56t_{\text{day}}) + \frac{\ln(1 + 0.34t_{\text{day}}^{0.74})}{0.34t_{\text{day}}^{0.74}} \right] , \quad (14)$$

where $t_0 = 1.3$ s, $\sigma = 0.11$ s, and $t_{\text{day}} = t/1$ day. The second term represents the adiabatic cooling of the ejecta, and it can be simplified by using the relation $R_i = v_i t$ as $-E_{i,j}/t$. The last term represents the energy that is carried out by emission, or the luminosity. It can be estimated by:

$$L_{i,j} = \frac{E_{i,j}}{\max[t_{\text{d}}^{i,j}, t_{\text{lc}}^i]} , \quad (15)$$

where the light-crossing time $t_{\text{lc}}^i = R_i/c$, and the photon diffusion time scale:

$$t_{\text{d}}^i \approx \frac{3\kappa^j}{\Delta\Omega R_i c} m_{\text{ex}}^{i,j} . \quad (16)$$

The diffusion time scale depends on the opacity of the ejecta κ^j , which is θ -dependent in our model. The $m_{\text{ex}}^{i,j}$ denotes the exterior mass of the patch, which sums the mass of the exterior of the i th shell for the j th patch.

By solving Eq. (13) and summing the luminosity of each shells for a specific patch and at a specific time step, we obtain the bolometric luminosity as a function of time:

$$L_{\text{bol}}^j = \sum_i L_{i,j} . \quad (17)$$

Additionally, the blackbody spectrum is assumed for the emission and the effective temperature can be calculated through this bolometric luminosity:

$$T_{\text{eff}}^j = \left(\frac{L_{\text{bol}}^j}{\sigma_{\text{SB}} \Delta \Omega R_{\text{ph}}^2} \right)^{1/4}, \quad (18)$$

where σ_{SB} is the Stephan-Boltzmann constant and R_{ph} is the radius of the photosphere, which is defined as the radius where the exterior optical depth $\tau_{R_{\text{max}}-R_{\text{ph}}}$ is unitary. This radius can be calculated analytically with the density distribution Eq. (12) as

$$R_{\text{ph}}^\tau = \left[R_{\text{max}}^{1-\delta} - \frac{4\pi}{M_{\text{ej}}\kappa} \frac{1-\delta}{3-\delta} (R_{\text{max}}^{3-\delta} - R_{\text{min}}^{3-\delta}) \right]^{\frac{1}{1-\delta}} \quad (19)$$

However, R_{ph}^τ may be smaller than R_{min} at the later time of evolution. We, therefore, define this photosphere radius as $R_{\text{ph}} = \max[R_{\text{ph}}^\tau, R_{\text{min}}]$. Eventually, the flux with frequency ν that is measured by the observer is obtained by summing up the contributions from all the rays

$$F_\nu = \frac{2h\nu^3}{c^2} \int_{\mathbf{n} \cdot \mathbf{n}_\Omega > 0} \frac{1}{\exp(h\nu/kT_{\text{eff}}) - 1} \frac{R_{\text{ph}}^2}{D^2} \mathbf{n} \cdot d\Omega, \quad (20)$$

where \mathbf{n} and \mathbf{n}_Ω are the unit vector along the line of sight, and the unit vector of the solid angle, respectively. Subsequently, we determine the monochromatic AB magnitude by $M_\nu = -2.5 \log_{10}(F_\nu/3631J)$.

Having determined the models for describing the EOS and kilonovae, we will perform the Bayesian analysis of the EOS by exploiting the data of AT2017gfo (Villar et al. 2017), GW170817 (Abbott et al. 2019), and NICER pulsars (Miller et al. 2019; Riley et al. 2019a; Miller et al. 2021; Riley et al. 2021a). Before that, an introduction of the details of Bayesian analysis will be presented in the next section.

3. OBSERVATIONAL CONSTRAINTS AND BAYESIAN ANALYSIS

Given a model hypothesis with a set of parameters $\boldsymbol{\theta}$, and some data d , the posterior probability can be obtained by applying the Bayes theorem,

$$p(\boldsymbol{\theta}|d) = \frac{\mathcal{L}(d|\boldsymbol{\theta})p(\boldsymbol{\theta})}{\int \mathcal{L}(d|\boldsymbol{\theta})p(\boldsymbol{\theta})d\boldsymbol{\theta}}, \quad (21)$$

where $\mathcal{L}(d|\boldsymbol{\theta})$ denotes the likelihood of the data d given a set of parameters $\boldsymbol{\theta}$ and their corresponding prior probability $p(\boldsymbol{\theta})$. The denominator is the evidence of data d and acts as a normalization factor. The evidence can be obtained by integrating the numerator all over the

Table 1. All of the parameters in the models and Bayesian analysis. Some of the parameters are not put into the analysis and sampling, and their prior distributions are denoted as Fixed. The log represent the uniform distribution of its logarithmic value, and the Constrained Uniform of the κ parameter denotes the uniform prior with the constrained condition $\kappa_{\text{high}} > \kappa_{\text{low}}$.

The parameters and priors of EOS				
Parameters	Unit	Prior	Minimum	Maximum
n_0	fm^{-3}	Fixed	0.16	0.16
E/A	MeV	Fixed	-16	-16
J_0	MeV	Uniform	30	35
K_0	MeV	Uniform	220	280
L_0	MeV	Uniform	20	85
$M_{\text{N}}^*/M_{\text{N}}$	-	Uniform	0.65	0.80

The parameters and priors of ejecta and the binary				
Parameters	Unit	Prior	Minimum	Maximum
\mathcal{M}	M_\odot	Uniform	1.18	1.21
q	-	Uniform	1	2
M_{ej}	M_\odot	Uniform	0.001	0.01
δ	-	Uniform	1	3
v_{min}	c	Uniform	0.01	0.15
v_{max}	c	Uniform	0.18	0.65
κ_{low}	cm g^{-1}	Cons. Uniform	0.1	30
κ_{high}	cm g^{-1}	Cons. Uniform	0.1	30
D	Mpc	Fixed	40	40
θ_{view}	Rad	Fixed	$\pi/6$	$\pi/6$

The central pressure of NICER sources				
Parameters	Unit	Prior	Minimum	Maximum
p_{c_1}	10^{34} dyn/cm^2	log	2.774	122.051
p_{c}	10^{34} dyn/cm^2	log	2.774	122.051

Three additional parameters to denote the deviations of quasi-universal relations for modelling kilonova				
Parameters	Unit	Prior	Mean	Deviation
α_m	-	Gaussian	0	0.2
α_v	-	Gaussian	0	0.2
α_e	-	Gaussian	0	0.2

parameter space. In reality, however, the parameter space has a non-trivial number of dimensions, and may lead to a severe problem that is often referred to as “the curse of dimensionality”. One can only resort to the statistical computational techniques, e.g., Markov Chain Monte Carlo or Nested Sampling methods, to approximate the evidence or the marginalized distributions. In our analysis, the python package BILBY (Ashton et al. 2019; Romero-Shaw et al. 2020) and the nested sampler pymultinest (Buchner et al. 2014) will be implemented to generate the posterior samples and estimate the marginalized distributions.

To incorporate the data of the kilonova light curve, the gravitational wave, and the NICER mass-radius measurements, we take the total likelihood function as the form of

$$\mathcal{L}(d|\boldsymbol{\theta}) = \mathcal{L}_{\text{AT2017gfo}} \times \mathcal{L}_{\text{GW170817}} \times \mathcal{L}_{\text{NICER}} . \quad (22)$$

More details of the likelihood are described below in Sec. 3.2.

3.1. Parameters and priors

As explained above in Sec. 2.1, the parameters of RMF models can be directly related to the saturation properties of nuclear matter. Therefore, the six saturation properties will be treated as free parameters in our Bayesian analysis. In practice, the first two properties, n_0 and E/A are well determined and have much smaller uncertainties compared with the rest four properties. We fix their value to be $n_0 = 0.16 \text{ fm}^{-3}$ and $E/A = 16 \text{ MeV}$. The prior distribution of the rest four properties are denoted as $\boldsymbol{\theta}_{\text{eos}}$ and are set as uniform distribution with the ranges displayed in Table 1

Furthermore, there are eight parameters in our kilonova model: The ejected mass M_{ej} , the index of the mass distribution δ , the minimal and maximal velocity v_{min} and v_{max} , the low and high opacity value κ_{low} and κ_{high} , the luminosity distance of the source D and the viewing angle θ_{view} . In our analysis, the distance and viewing angle are fixed as $D = 40 \text{ Mpc}$ and $\theta_{\text{view}} = \pi/6$. We denote the rest six parameters as $\boldsymbol{\theta}_{\text{kn}}$ and compute their posterior distribution in the following analysis.

The six input kilonova parameters $\boldsymbol{\theta}_{\text{kn}}$ describing the properties of ejecta do relate to the binary parameters. Indeed, the quasi-universal relations are extracted by fitting the data of simulations (see Nedora et al. 2021, 2022, for more details) and the ejected mass M_{ej} , the mean velocity v_{mean} and the electron fraction Y_e are expressed as functions of binary parameters (mass ratio q and reduced tidal parameter $\tilde{\Lambda}$). However, these relations are not exact and deviations from the fitted formulations are expected in realistic situations. We introduce three deviation parameters to account for the

uncertainty of the relations accordingly (Breschi et al. 2021). Consequently, the M_{ej} , v_{mean} and Y_e are expressed with three additional deviation parameters α_m , α_v and α_e as

$$\log_{10} M_{\text{ej}} = (1 + \alpha_m) \log_{10} M_{\text{ej}}^{\text{fit}}(q, \tilde{\Lambda}) , \quad (23)$$

$$v_{\text{mean}} = (1 + \alpha_v) v_{\text{mean}}^{\text{fit}}(q, \tilde{\Lambda}) , \quad (24)$$

$$Y_e = (1 + \alpha_e) Y_e^{\text{fit}}(q, \tilde{\Lambda}) . \quad (25)$$

The three deviation parameters $\boldsymbol{\theta}_{\text{dev}} = (\alpha_m, \alpha_v, \alpha_e)$ will be treated as input parameters in our Bayesian analysis, and their priors follow the Gaussian distribution with vanished means and standard deviations of 0.2.

In our kilonova models that take v_{min} and v_{max} as the input parameters, the mean velocity can be expressed in terms of the minimal and maximal velocity as

$$v_{\text{mean}} = \frac{(3 - \delta)(v_{\text{max}}^{4-\delta} - v_{\text{min}}^{4-\delta})}{(4 - \delta)(v_{\text{max}}^{3-\delta} - v_{\text{min}}^{3-\delta})} . \quad (26)$$

The electron fraction Y_e can be mapped into the mean opacity $\bar{\kappa}$ of the ejecta by the relation in Tanaka et al. (2020). The $\bar{\kappa}$ can be written as

$$\bar{\kappa} = \frac{\sqrt{2}}{2} \kappa_{\text{high}} + (1 - \frac{\sqrt{2}}{2}) \kappa_{\text{low}} . \quad (27)$$

Meanwhile, once an EOS is determined from the EOS parameters $\boldsymbol{\theta}$, the binary properties (mass ratio q and $\tilde{\Lambda}$) can be determined with given masses. Therefore, all of the kilonova parameters $\boldsymbol{\theta}_{\text{kn}}$ can be mapped into the EOS parameters $\boldsymbol{\theta}_{\text{eos}}$ with three deviation parameters and two binary properties parameters (we use the mass ratio q and the chirp mass \mathcal{M} in our analysis) by utilizing these above relations.

Finally, two additional parameters $\boldsymbol{\theta}_{\text{nicer}}$ are required for the NICER data, which represent the central pressure of PSR J0030+0451 and PSR J0740+6620. All of the parameters and their prior distributions are summarily displayed in Table 1.

3.2. The observational data and likelihood

3.2.1. AT2017gfo

The observed light curves of AT2017gfo (Villar et al. 2017) will be fitted by our kilonova model. In reproducing the light curve of AT2017gfo, we only consider the dynamical ejecta as the source of r -process nucleosynthesis, since the effects of EOS on other parts of ejecta are mild (see e.g., Perego et al. 2017; Yu et al. 2018; Ren et al. 2019; Breschi et al. 2021). In Fig. 1, we plot the light curves of the kilonova model with the best-fitting parameters of $\boldsymbol{\theta}_{\text{kn}}$. The observational data (circles) or limits (triangles) are taken from Villar et al. (2017).

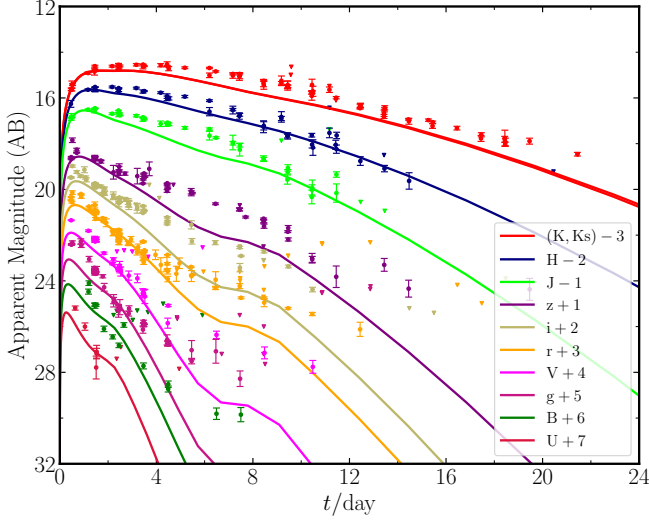


Figure 1. The light curves of the kilonova emission with the best-fitting parameters of θ_{kn} , the solid lines with different color represent the predictions of the model of various bands. The observational data (circles) or limits (triangles) are taken from Villar et al. (2017).

Table 2. The posterior results of the kilonova model parameters θ_{kn} , the best fit values, the median value, and the 90% confidence interval for each parameter are displayed.

Parameters	Best fit	Median(90%)
$M_{\text{ej}} (10^{-2} M_{\odot})$	2.5977	$2.5972^{+0.0115}_{-0.0109}$
δ	1.3078	$1.3081^{+0.0091}_{-0.0095}$
$v_{\text{min}}(c)$	0.1061	$0.1061^{+0.0004}_{-0.0004}$
$v_{\text{max}}(c)$	0.5066	$0.5065^{+0.0037}_{-0.0036}$
$\kappa_{\text{low}}(\text{cm g}^{-1})$	0.7844	$0.7843^{+0.0044}_{-0.0041}$
$\kappa_{\text{high}}(\text{cm g}^{-1})$	6.9509	$6.9487^{+0.0495}_{-0.0462}$

Note that the solid lines that represent the model predictions deviate from the observational data significantly after 4 days of the merger event for most of the bands (only K, H, J bands are compatible). This might be the consequence that only two components (red and blue) are taken into account in our model. As generally believed, a third component should be incorporated to account for it (e.g., Perego et al. 2017; Villar et al. 2017; Yu et al. 2018; Ren et al. 2019; Breschi et al. 2021; Qi et al. 2022), including the energy or material injection from the central black hole hyperaccretion systems or magnetars, which is independent to the EOS. Therefore we will not address further in the following.

After obtaining the posterior samples of kilonova parameters θ_{kn} , we approximate their posterior distribution with the Gaussian kernel density estimation

(KDE). In the following, the posterior distribution will be treated as the likelihood of the EOS parameters θ_{eos} and the deviation parameters θ_{dev} .

3.2.2. GW170817

The GW170817 likelihood is calculated through a high-precision interpolation of the likelihood developed in Hernandez Vivanco et al. (2020) from fitting the strain data released by LIGO/Virgo, which is encapsulated in the python package `toast`,

$$\mathcal{L}_{\text{GW170817}} = F(\Lambda_1, \Lambda_2, \mathcal{M}, q), \quad (28)$$

where the chirp mass is $\mathcal{M} = (M_1 M_2)^{3/5} / (M_1 + M_2)^{1/5}$, the mass ratio is $q = M_1 / M_2$, and $\Lambda_1(M_1)$ and $\Lambda_2(M_2)$ denote the tidal deformability (mass) of the individual star, respectively. Λ_1 and Λ_2 are connected with the reduced tidal deformability $\tilde{\Lambda}$ by

$$\tilde{\Lambda} = \frac{16}{13} \frac{(q + 12)q^4 \Lambda_1 + (1 + 12q)\Lambda_2}{(1 + q)^5}. \quad (29)$$

The tidal deformability, mass, and radius of a star can be computed by solving the perturbed tidal field equation (Flanagan & Hinderer 2008; Hinderer 2008; Hinderer et al. 2010) and the TOV equation simultaneously. Once the EOS and the central pressure of the star are determined, one can integrate both equations from the stellar center to the surface, where the pressure vanishes.

3.2.3. PSR J0030+0451 and PSR J0740+6620

The mass-radius measurements of two pulsars PSR J0030+0451 and PSR J0740+6620 by NICER collaborations have set strong constraints on the EOS. At 68% confidence level, the mass and radius of PSR J0030+0451 are $M = 1.34^{+0.15}_{-0.16} M_{\odot}$, $R = 12.71^{+1.14}_{-1.19}$ km by Riley et al. (2019a), or $M = 1.44^{+0.15}_{-0.14} M_{\odot}$, $R = 13.02^{+1.24}_{-1.06}$ km by Miller et al. (2019); and the results of PSR J0740+6620 are $M = 2.072^{+0.067}_{-0.066} M_{\odot}$, $R = 12.39^{+1.30}_{-0.98}$ km by Miller et al. (2021), or $M = 2.062^{+0.090}_{-0.091} M_{\odot}$, $R = 13.71^{+2.61}_{-1.50}$ km by Miller et al. (2021). We implement ST+PST model samples of PSR J0030+0451 (Riley et al. 2019b) and the NICER x XMM samples of PSR J0740+6620 (Riley et al. 2021b) with the KDE methods to generate the posterior distributions, which will be treated as the likelihood in our analysis. Note that the central pressure for these two pulsars is included and treated as input parameters when calculating the NICER likelihood. The masses and radii will be computed by solving the TOV equation with the EOS with given central pressures.

4. RESULTS AND DISCUSSIONS

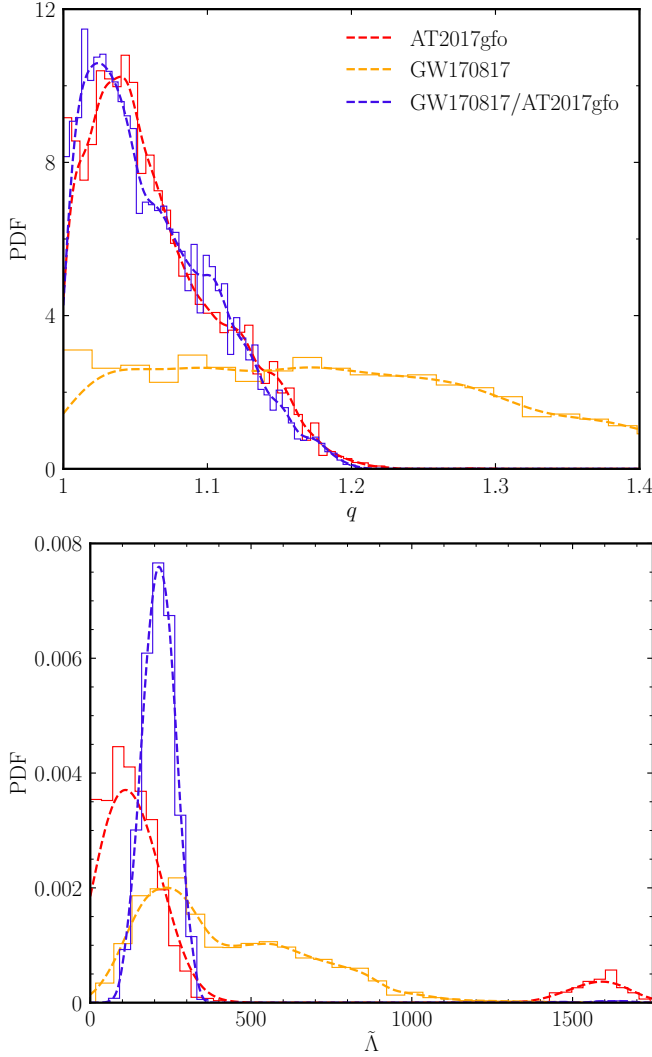


Figure 2. The posterior distributions of q (upper) and $\tilde{\Lambda}$ (lower) for AT2017gfo (red), GW170817 (orange) and the AT2017gfo/GW170817 (blue) result. The solid lines represent the histogram of the posterior samples, and the dash lines are smoothed by the Gaussian KDE methods from the histogram.

Table 3. The median value and 90% confidence interval of q and $\tilde{\Lambda}$ for different likelihood data. The large value of the confidence interval upper limit of $\tilde{\Lambda}$ for AT2017gfo is the result of the second peak in the posterior distributions.

Likelihood	q	$\tilde{\Lambda}$
AT2017gfo	$1.0530^{+0.0972}_{-0.0476}$	$127.1565^{+1444.4892}_{-112.5691}$
GW170817	$1.1871^{+0.2656}_{-0.1706}$	$350.6256^{+530.0389}_{-243.0834}$
AT2017gfo/GW170817	$1.0513^{+0.0916}_{-0.0452}$	$213.5724^{+80.5000}_{-80.1237}$

The EOS is connected with the ejecta properties through the quasi-universal relations, which are the

functions of the mass ratio q and the reduced tidal deformability $\tilde{\Lambda}$. In our analysis, the parameters of kilonova model θ_{kn} will first be sampled. Their posterior results are displayed in Table 2. The posterior distributions of the ejecta parameters will be approximated by implementing the Gaussian KDE method, and these posterior will further be used as the likelihood of kilonova observations when sampling the binary parameters or EOS parameters.

4.1. GW170817: mass ratio and tidal deformability

The quasi-universal relations with their deviations (23)–(25) describe the ejecta properties in terms of the binary parameters (the mass ratio q and the reduced tidal deformability $\tilde{\Lambda}$). We first compute the posterior samples of q and $\tilde{\Lambda}$ by implementing the nested sampler, and compare the results to those of AT2017gfo, GW170817 and AT2017gfo/GW170817 in Fig. 2. We report in detail the median values and the 90% confidence intervals in Table 3.

Fig. 2 reports the posterior distributions of the mass ratio q (upper panel) and reduced tidal deformability $\tilde{\Lambda}$ (lower panel) by fitting the AT2017gfo light curve data, the GW170817 likelihood, and the combined data of kilonova and gravitational wave, and they are represented by the red, orange and blue lines, respectively. The solid lines represent the histogram of the samples and the dashed lines represent the distributions fitted by Gaussian KDE. Note that the KDE results of distributions deviate from the histogram when q is close to 1, for a stiff boundary are set at $q = 1$ and the cases with $q < 1$ do not exist. However, the Gaussian KDE function may extend to the region of $q < 1$ and result in a decline close to $q = 1$. In the upper panel of the distributions of mass ratio, it is seen that in comparison to the results from the GW170817 data, AT2017gfo favors a smaller mass ratio. In the lower panel of the $\tilde{\Lambda}$ distributions, an interesting aspect of the kilonova data is reported. The result of the kilonova fitting displays a bimodal structure (Breschi et al. 2021): The first and the dominant peak locate around $\tilde{\Lambda} = 114$, while the secondary one is around $\tilde{\Lambda} = 1610$. Because of the second peak, the 90% confidence interval upper limit of $\tilde{\Lambda}$ is considerably larger than the GW170817 and GW170817/AT2017gfo results (shown in Table 3). Moreover, the first peak is close to that of GW170817 posterior distribution and results in a significant enhancement around $\tilde{\Lambda} = 213$ region in the result of the combined data. Nevertheless, the secondary peak is suppressed by the GW170817 data and disappeared. In spite of the consistency of the location of the dominant peaks, GW170817 results show a longer tail with a larger value of $\tilde{\Lambda}$. Consequently,

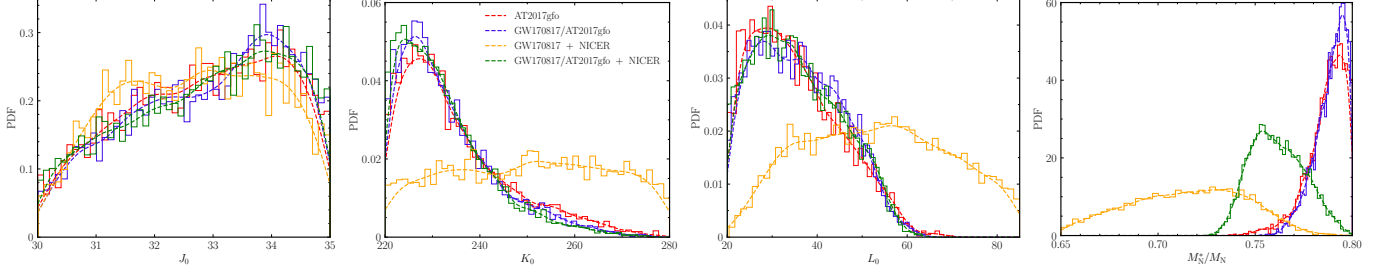


Figure 3. The posterior distributions of RMF EOS parameters θ_{eos} . Be the same with Fig. 2, the histogram of the posterior samples and the smoothed distribution functions by the Gaussian KDE are represented by the solid and dash lines, respectively. The results from different analyses, AT2017gfo (red), GW170817/AT2017gfo (blue), GW170817 + NICER (orange) and GW170817/AT2017gfo + NICER (green), are denoted by different colors.

Table 4. 90% confidence intervals of the EOS parameters θ_{eos} , or the saturation properties for nuclear matter, and the stellar properties constrained by four different analyses within the RMF framework.

Parameters	AT2017gf	GW170817/AT2017gf	GW170817+NICER	GW170817/AT2017gf+NICER
J_0 (MeV)	$32.9321^{+1.8031}_{-2.3807}$	$33.0866^{+1.6679}_{-2.4922}$	$32.7278^{+1.9317}_{-2.1386}$	$33.0410^{+1.7229}_{-2.5494}$
K_0 (MeV)	$231.5976^{+27.6173}_{-10.1760}$	$230.5804^{+23.9437}_{-9.2084}$	$250.8818^{+25.1076}_{-27.2728}$	$230.2890^{+22.0389}_{-9.0966}$
L_0 (MeV)	$33.7546^{+19.8140}_{-11.6658}$	$35.3533^{+17.1443}_{-13.1968}$	$53.1642^{+26.3730}_{-24.9273}$	$34.4599^{+18.2543}_{-12.5515}$
M_N^*/M_N	$0.7887^{+0.0100}_{-0.0211}$	$0.7904^{+0.0083}_{-0.0172}$	$0.7166^{+0.0446}_{-0.0517}$	$0.7604^{+0.0250}_{-0.0198}$
$R_{1.4}$ (km)	$11.4107^{+0.2875}_{-0.2229}$	$11.3930^{+0.2364}_{-0.2123}$	$12.3821^{+0.5311}_{-0.5639}$	$11.6367^{+0.2121}_{-0.2312}$
$\Lambda_{1.4}$	$255.0494^{+41.1186}_{-26.4017}$	$251.2908^{+32.4407}_{-25.4602}$	$440.8698^{+123.4322}_{-107.7413}$	$300.2940^{+26.9738}_{-36.7643}$

the AT2017gfo data strongly favor a smaller tidal deformability and softer EOS, which will be shown in the following sections.

4.2. The nuclear EOS parameters and neutron star properties

The EOS is specified by four parameters in our analyses, which are the symmetry energy J_0 , incompressibility K_0 , symmetry energy slope L_0 and effective mass ratio M_N^*/M_N . In our process of sampling, we first calculate the coupling constants from these saturations properties, and calculate by solving the equations of motion (2)–(4) the neutron star core EOS after adding the lepton contribution. We then join the core EOS with the usual BPS crust one (Baym et al. 1971). The mass, radius and tidal deformability of neutron stars will be obtained with the whole stellar EOS and the likelihood of various cases are yielded.

We report the posterior distributions of EOS parameters θ_{eos} in Fig. 3, and collect the median values and the 90% confidence intervals in Table 4. The results of four different analyses with the data of AT2017gfo (red), GW170817/AT2017gfo (blue), GW170817 + NICER (orange) and GW170817/AT2017gfo + NICER (green) are reported in Fig. 3. Same with Fig. 2, the histograms are denoted by the solid lines and the approximated distributions of KDE are denoted by dash lines.

The symmetry energy reported in Fig. 3 (leftmost panel) from different analyses shows similar distributions. This similarity can also be found for the confidence intervals in Table 4, and representing the insensitivity of symmetry energy J_0 on these observational data. All of our analyses favor smaller incompressibility except for the GW170817 + NICER (orange) (see the second panel of Fig. 3). For example, the median value of K_0 is around 250 MeV for the GW170817 + NICER case, while it is around 230 MeV for the other three analyses. Such a deviation is a consequence of the massive pulsar PSR J0740+6620 from NICER, which strongly favors a stiff EOS and hence a larger K_0 . On the contrary, the dominate peaks in $\tilde{\Lambda}$ distribution (see Fig. 2) of both GW170817 and AT2017gfo (red and blue) analyses imply a preference for soft EOS and a smaller radius for neutron stars. This difference between GW170817/AT2017gfo and NICER can also be found in the distributions of symmetry energy slope L_0 and effective mass ratio M_N^*/M_N . The L_0 of GW170817 + NICER analysis tends to be a larger value and implies a larger radius of neutron star (Zhu et al. 2018). Similarly, a larger nucleon effective mass, which is preferred by the AT2017gfo and GW170817/AT2017gfo analyses results in a softer EOS (Hornick et al. 2018). The introduction of the NICER observational data in our likelihood requires stiffer EOS and smaller effective mass.

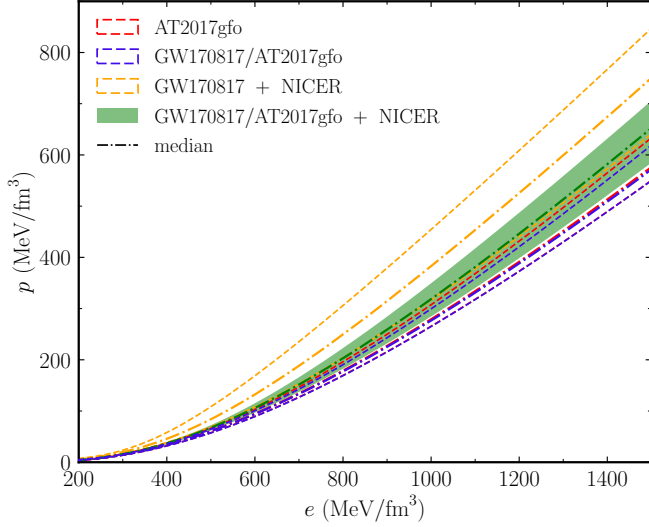


Figure 4. The 90% confidence interval of EOS for all four analyses. The green shaded region represents the result of GW170817/AT2017gfo + NICER analysis, while other contours are represented by dash lines. The colors for each analyses are the same with the previous figure. The dash-dot lines denote the median results of the posterior distributions.

Therefore, the distribution of GW170817 + NICER (orange) favors a smaller effective mass, and the ratio decreases from 0.79 of GW170817 and AT2017gfo analyses to 0.72 of GW170817 + NICER. Finally, a trade-off of effective mass is achieved by the GW170817/AT2017gfo + NICER analyses that balanced the soft EOS preference of GW170817/AT2017gfo and stiff one of PSR J0740+6620 in NICER data.

Fig. 4 compares and contrasts the 90% confidence intervals of the EOSs for all the analyses. The contour of GW170817/AT2017gfo + NICER analysis is denoted by the green shaded region, while the other contours are denoted by the dash lines. The median results for each posterior distribution are denoted by the dash-dot lines with the corresponding colors. The results of the EOS confidence interval are consistent with the saturation properties distributions and our previous discussions. Note that the secondary peak in $\tilde{\Lambda}$ disappeared in the distribution of EOS and saturation properties for AT2017gfo analysis. The large $\tilde{\Lambda}$ value of the secondary peak implies an unrealistically stiff EOSs, which are disfavored by the nuclear experimental results (e.g., Drischler et al. 2020; Zhang et al. 2021). For example, in the current framework of the RMF model, an EOS with $E_{\text{sym}} = 43$ MeV, $K = 300$ MeV, $L = 142$ MeV, $M_N^*/M_N = 0.55$ could result in $\tilde{\Lambda} = 1450$.

Moreover, the interval contours and the median lines of AT2017gfo and GW170817/AT2017gfo are almost overlapping with each other. Reminding the proximity

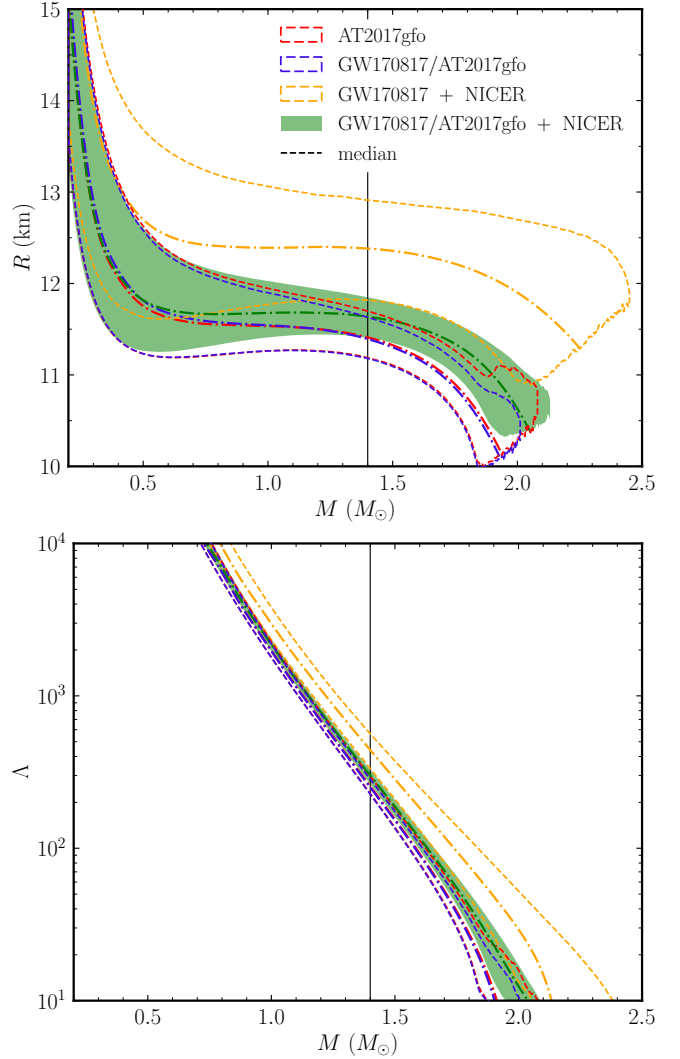


Figure 5. Same with Fig. 4, but for the radius (upper panel) and tidal deformability (lower panel) as functions of the stellar mass. The vertical black line is the $1.4 M_{\odot}$ line.

of the dominate peak of $\tilde{\Lambda}$ distributions from AT2017gfo and GW170817 analyses in Fig. 2, this similarity on EOS is the result of that, and implies the consistency of AT2017gfo and GW170817 data. On the other hand, the analyses of the NICER data favor stiffer EOS because of the massive pulsar. The medium region that fulfills the small $\tilde{\Lambda}$ and large maximum mass M_{TOV} is significantly enhanced in the distribution of the analysis that takes all data into account. Meanwhile, the very soft and very stiff EOS is disfavored.

Finally, we report the mass-radius relations and the tidal deformability intervals of each analysis in Fig. 5, and display the radius and tidal deformability of $1.4 M_{\odot}$ stars $R_{1.4}$ and $\Lambda_{1.4}$ in the last two rows of Table 4, respectively. The analyses with GW170817 and AT2017gfo give smaller radius for stars around $1.4 M_{\odot}$

compared with the analyses with NICER data. The median value of $R_{1.4}$ increases from ~ 11.4 km for AT2017gfo and GW170817/AT2017gfo to 12.4 km for GW170817 + NICER, and further decreases to 11.6 km for GW170817/AT2017gfo + NICER because of the trade-off. We mention here that the radius results are similar to the ones obtained with a chiral effective-field-theory description of nuclear matter (Capano et al. 2020). The tidal deformability $\Lambda_{1.4}$ has the similar behavior (increases from ~ 250 to 440 and further goes down to 300) due to the positive correlation between $\Lambda_{1.4}$ and $R_{1.4}$ (e.g., Lim & Holt 2018).

5. CONCLUSIONS

Even since the first detection of the multimessenger signal of the GW170817 binary neutron star merger, a large number of works have investigated its implications on the neutron star EOS. The matter effects of the binary system imprinted into the gravitational wave signal as the tidal deformability contributions, and one may extract from it and constrain the EOS by analyzing the GW signals. On the other hand, the transient kilonova event of AT2017g can also shed light on the neutron star EOS through the properties of dynamical ejecta.

In this work, we implemented the quasi-universal relations between the binary properties (the mass ratio q and reduced tidal deformability $\tilde{\Lambda}$) and the ejecta properties (the ejected mass, velocity, and electron fraction), and combined the observational data of AT2017gfo to constrain the neutron star EOS. The reduced tidal deformability of binary can be directly related to the saturation properties of nuclear matter in the framework of the RMF model. Thereafter, we performed the Bayesian analysis of the EOS and the saturation

properties (the symmetry energy J_0 , incompressibility K_0 , symmetry energy slope L_0 , and effective mass ratio M_N^*/M_N) with the AT2017gfo light curve data. Our analysis shows a bimodal structure of the $\tilde{\Lambda}$ distribution, where the dominant peak corresponds to softer EOS and a smaller radius of stars. This dominant peak is enhanced by the GW170817 results, while the second peak is suppressed and disappeared in the distribution of GW170817/AT2017gfo.

We proceed to perform joint analyses with various observational data combinations (GW170817/AT2017gfo, GW170817 + NICER, and GW170817/AT2017gfo + NICER). The 90% confidence interval of EOS of AT2017gfo and GW170817/AT2017gfo were almost overlapping with each other, implying the consistency of GW170817 and AT2017gfo. However, the introduction of NICER data makes the posterior distributions strongly favor stiff EOS with a larger stellar radius, since the massive pulsar PSR J0740+6620 in the NICER data demands stiff EOSs to be consistent with it. As a result, both the very stiff and very soft EOSs are excluded for their incapability to reproduce the AT2017gfo data or PSR J0740+6620 data. When combining all observational data, the nuclear matter properties at saturation are found to be $J_0 = 33.0410^{+1.7229}_{-2.5494}$ MeV, $K_0 = 230.2890^{+22.0389}_{-9.0966}$ MeV, $L_0 = 34.4599^{+18.2543}_{-12.5515}$ MeV and $M_N^*/M_N = 0.7604^{+0.0250}_{-0.0198}$, at 90% confidence level. Correspondingly, the radius and the tidal deformability for $1.4 M_\odot$ neutron stars are $11.6367^{+0.2121}_{-0.2312}$ km and $300.2940^{+26.9738}_{-36.7643}$, respectively. More future joint multimessenger observations on neutron stars, binary evolution, and their mergers are expected to further constrain their EOS.

APPENDIX

A. DETAILED DERIVATION OF NUCLEAR MATTER PROPERTIES FROM RMF MODEL PARAMETERS

We sum up the energy density and pressure expressions (6) – (7) at saturation density ($p = 0$) to yield a simplified expression:

$$e + p = (E/A + M_N)n_0 = \sum_{i=n,p} e_{\text{kin}}^i + \sum_{i=n,p} p_{\text{kin}}^i + g_\omega \omega n_0. \quad (\text{A1})$$

The left-hand-side is known from E/A and n_0 , and the kinetic terms only depends on fermi momentum p_F and effective mass. Combine this equation with the ω equation of motion, we can express ω and g_ω in terms of the known quantities

$$\omega = \sqrt{\frac{(E/A + M_N)n_0 - \sum_i (e_{\text{kin}} + p_{\text{kin}})}{m_\omega^2}}, \quad (\text{A2})$$

$$g_\omega = \frac{m_\omega^2 \omega}{n_0}. \quad (\text{A3})$$

The expressions of Λ_v and g_ρ (ρ vanishes for symmetric nuclear matter) can also be obtained in the same way by combining eqs. (4), (8) and (10)

$$\Lambda_v = -\frac{m_\omega^2 \alpha}{3\beta^2 g_\omega^3 \omega n_0^2}, \quad (\text{A4})$$

$$g_\rho^q = \sqrt{\frac{m_\rho^2}{\beta^{-1} - \Lambda_v (g_\omega \omega)^2}}. \quad (\text{A5})$$

where α and β is written as

$$\alpha = L_0 - 3J_0 - \frac{1}{2} \left(\frac{3\pi^2}{2} n_0 \right)^{2/3} \frac{1}{E_F} \times \left(\frac{g_\omega^2}{m_\omega^2 + \Lambda_v (g_\omega g_\rho \rho)^2} \frac{n_0}{E_F} - \frac{K_0}{9E_F} - \frac{1}{3} \right), \quad (\text{A6})$$

$$\beta = \frac{2J_0}{n_0} - \frac{p_F^2}{3E_F n_0}. \quad (\text{A7})$$

The last three parameters determination rely on eqs. (7), (2) and the derivative of (2). Their expressions can be written as

$$\sigma = \sqrt{\frac{C - 6B + 12A}{m_\sigma^2}}, \quad (\text{A8})$$

$$g_2 = \frac{-3C + 15B - 24A}{\sigma^3}, \quad (\text{A9})$$

$$g_3 = \frac{2C - 8B + 12A}{\sigma^4}, \quad (\text{A10})$$

$$g_\sigma = \frac{(g_\sigma \sigma)}{\sigma}, \quad (\text{A11})$$

where A , B and C are

$$A = \sum_{i=n,p} p_{\text{kin}}^i + \frac{1}{2} m_\omega^2 \omega^2, \quad (\text{A12})$$

$$B = (g_\sigma \sigma) n_s, \quad (\text{A13})$$

$$C = -(g_\sigma \sigma)^2 \left[\frac{\partial n_s}{dM_N^*} + \frac{\partial n_s}{\partial p_F} / \frac{\partial M_N^*}{dp_F} \right]. \quad (\text{A14})$$

In these expressions, $(g_\sigma \sigma)$ can be evaluated by $g_\sigma \sigma = M_N - M_N^*$, $\partial M_N^* / dp_F$ is obtained from K_0 .

ACKNOWLEDGEMENTS

We are thankful to Jinping Zhu, Yanqing Qi, Enping Zhou and the XMU neutron star group for the helpful input and discussions. This work was supported by National SKA Program of China (No. 2020SKA0120300), the National Natural Science Foundation of China (Grant Nos. 12273028, 12103033, 12173031, and 12221003), the Youth Innovation Fund of Xiamen (No. 3502Z20206061) and the China national postdoctoral program for innovation talents (No. BX20220207).

REFERENCES

- Abbott, B. P., Abbott, R., Abbott, T. D., et al. 2017, Phys. Rev. Lett., 119, 161101, doi: [10.1103/PhysRevLett.119.161101](https://doi.org/10.1103/PhysRevLett.119.161101)
- , 2018, Physical Review Letters, 121, 161101, doi: [10.1103/PhysRevLett.121.161101](https://doi.org/10.1103/PhysRevLett.121.161101)
- , 2019, Physical Review X, 9, 031040, doi: [10.1103/PhysRevX.9.031040](https://doi.org/10.1103/PhysRevX.9.031040)

- Andreoni, I., Ackley, K., Cooke, J., et al. 2017, *PASA*, 34, e069, doi: [10.1017/pasa.2017.65](https://doi.org/10.1017/pasa.2017.65)
- Arcavi, I., Hosseinzadeh, G., Howell, D. A., et al. 2017, *Nature*, 551, 64, doi: [10.1038/nature24291](https://doi.org/10.1038/nature24291)
- Ashton, G., Hübner, M., Lasky, P. D., et al. 2019, *ApJS*, 241, 27, doi: [10.3847/1538-4365/ab06fc](https://doi.org/10.3847/1538-4365/ab06fc)
- Barnes, J., Kasen, D., Wu, M.-R., & Martínez-Pinedo, G. 2016, *Astrophys. J.*, 829, 110, doi: [10.3847/0004-637X/829/2/110](https://doi.org/10.3847/0004-637X/829/2/110)
- Baym, G., Pethick, C., & Sutherland, P. 1971, *Astrophys. J.*, 170, 299, doi: [10.1086/151216](https://doi.org/10.1086/151216)
- Bovard, L., Martin, D., Guercilena, F., et al. 2017, *Phys. Rev. D*, 96, 124005. <https://arxiv.org/abs/1709.09630>
- Breschi, M., Perego, A., Bernuzzi, S., et al. 2021, *MNRAS*, 505, 1661, doi: [10.1093/mnras/stab1287](https://doi.org/10.1093/mnras/stab1287)
- Buchner, J., Georgakakis, A., Nandra, K., et al. 2014, *A&A*, 564, A125, doi: [10.1051/0004-6361/201322971](https://doi.org/10.1051/0004-6361/201322971)
- Capano, C. D., Tews, I., Brown, S. M., et al. 2020, *Nature Astronomy*, 4, 625, doi: [10.1038/s41550-020-1014-6](https://doi.org/10.1038/s41550-020-1014-6)
- Coughlin, M. W., Dietrich, T., Margalit, B., & Metzger, B. D. 2019, *MNRAS*, 489, L91, doi: [10.1093/mnras/slz133](https://doi.org/10.1093/mnras/slz133)
- Coulter, D. A., Foley, R. J., Kilpatrick, C. D., et al. 2017, *Science*, 358, 1556, doi: [10.1126/science.aap9811](https://doi.org/10.1126/science.aap9811)
- Cowperthwaite, P. S., Berger, E., Villar, V. A., et al. 2017, *ApJL*, 848, L17, doi: [10.3847/2041-8213/aa8fc7](https://doi.org/10.3847/2041-8213/aa8fc7)
- De, S., Finstad, D., Lattimer, J. M., et al. 2018, *Physical Review Letters*, 121, 091102, doi: [10.1103/PhysRevLett.121.091102](https://doi.org/10.1103/PhysRevLett.121.091102)
- Díaz, M. C., Macri, L. M., Garcia Lambas, D., et al. 2017, *ApJL*, 848, L29, doi: [10.3847/2041-8213/aa9060](https://doi.org/10.3847/2041-8213/aa9060)
- Drishler, C., Furnstahl, R. J., Melendez, J. A., & Phillips, D. R. 2020, *PhRvL*, 125, 202702, doi: [10.1103/PhysRevLett.125.202702](https://doi.org/10.1103/PhysRevLett.125.202702)
- Drout, M. R., Piro, A. L., Shappee, B. J., et al. 2017, *Science*, 358, 1570, doi: [10.1126/science.aaq0049](https://doi.org/10.1126/science.aaq0049)
- Ecker, C., & Rezzolla, L. 2022, arXiv e-prints, arXiv:2207.04417. <https://arxiv.org/abs/2207.04417>
- Evans, P. A., Cenko, S. B., Kennea, J. A., et al. 2017, *Science*, 358, 1565, doi: [10.1126/science.aap9580](https://doi.org/10.1126/science.aap9580)
- Flanagan, É. É., & Hinderer, T. 2008, *Physical Review D*, 77, 021502, doi: [10.1103/PhysRevD.77.021502](https://doi.org/10.1103/PhysRevD.77.021502)
- Hernandez Vivanco, F., Smith, R., Thrane, E., & Lasky, P. D. 2020, *Mon. Not. R. Astron. Soc.*, 499, 5972, doi: [10.1093/mnras/staa3243](https://doi.org/10.1093/mnras/staa3243)
- Hinderer, T. 2008, *Astrophys. J.*, 677, 1216, doi: [10.1086/533487](https://doi.org/10.1086/533487)
- Hinderer, T., Lackey, B. D., Lang, R. N., & Read, J. S. 2010, *Phys. Rev. D*, 81, 123016, doi: [10.1103/PhysRevD.81.123016](https://doi.org/10.1103/PhysRevD.81.123016)
- Holmbeck, E. M., O’Shaughnessy, R., Delfavero, V., & Belczynski, K. 2022, *ApJ*, 926, 196, doi: [10.3847/1538-4357/ac490e](https://doi.org/10.3847/1538-4357/ac490e)
- Hornick, N., Tolos, L., Zacchi, A., Christian, J.-E., & Schaffner-Bielich, J. 2018, *PhRvC*, 98, 065804, doi: [10.1103/PhysRevC.98.065804](https://doi.org/10.1103/PhysRevC.98.065804)
- Hu, L., Wu, X., Andreoni, I., et al. 2017, *Science Bulletin*, 62, 1433, doi: [10.1016/j.scib.2017.10.006](https://doi.org/10.1016/j.scib.2017.10.006)
- Kasliwal, M. M., Nakar, E., Singer, L. P., et al. 2017, *Science*, 358, 1559, doi: [10.1126/science.aap9455](https://doi.org/10.1126/science.aap9455)
- Koliogiannis, P. S., & Moustakidis, C. C. 2019, *Ap&SS*, 364, 52, doi: [10.1007/s10509-019-3539-7](https://doi.org/10.1007/s10509-019-3539-7)
- Korobkin, O., Rosswog, S., Arcones, A., & Winteler, C. 2012, *Mon. Not. R. Astron. Soc.*, 426, 1940, doi: [10.1111/j.1365-2966.2012.21859.x](https://doi.org/10.1111/j.1365-2966.2012.21859.x)
- Lattimer, J. M., & Prakash, M. 2000, *Physics Reports*, 333, 121, doi: [10.1016/S0370-1573\(00\)00019-3](https://doi.org/10.1016/S0370-1573(00)00019-3)
- Li, A., Miao, Z., Han, S., & Zhang, B. 2021a, *ApJ*, 913, 27, doi: [10.3847/1538-4357/abf355](https://doi.org/10.3847/1538-4357/abf355)
- Li, A., Miao, Z. Q., Jiang, J. L., Tang, S. P., & Xu, R. X. 2021b, *MNRAS*, 506, 5916, doi: [10.1093/mnras/stab2029](https://doi.org/10.1093/mnras/stab2029)
- Li, A., Zhu, Z. Y., Zhou, E. P., et al. 2020, *Journal of High Energy Astrophysics*, 28, 19, doi: [10.1016/j.jheap.2020.07.001](https://doi.org/10.1016/j.jheap.2020.07.001)
- Li, B.-A., Chen, L.-W., & Ko, C. M. 2008, *Physics Reports*, 464, 113, doi: [10.1016/j.physrep.2008.04.005](https://doi.org/10.1016/j.physrep.2008.04.005)
- Lim, Y., & Holt, J. W. 2018, *Phys. Rev. Lett.*, 121, 062701, doi: [10.1103/PhysRevLett.121.062701](https://doi.org/10.1103/PhysRevLett.121.062701)
- Lindblom, L. 2010, *PhRvD*, 82, 103011, doi: [10.1103/PhysRevD.82.103011](https://doi.org/10.1103/PhysRevD.82.103011)
- Lipunov, V. M., Gorbvskoy, E., Kornilov, V. G., et al. 2017, *ApJL*, 850, L1, doi: [10.3847/2041-8213/aa92c0](https://doi.org/10.3847/2041-8213/aa92c0)
- Margalit, B., & Metzger, B. D. 2017, *Astrophys. J. Lett.*, 850, L19, doi: [10.3847/2041-8213/aa991c](https://doi.org/10.3847/2041-8213/aa991c)
- Metzger, B. D. 2017, *Living Reviews in Relativity*, 20, 3, doi: [10.1007/s41114-017-0006-z](https://doi.org/10.1007/s41114-017-0006-z)
- Miao, Z., Li, A., & Dai, Z.-G. 2022a, *MNRAS*, doi: [10.1093/mnras/stac2015](https://doi.org/10.1093/mnras/stac2015)
- Miao, Z., Li, A., Zhu, Z., & Han, S. 2020, *ApJ*, 904, 103, doi: [10.3847/1538-4357/abbd41](https://doi.org/10.3847/1538-4357/abbd41)
- Miao, Z., Zhu, Y., Li, A., & Huang, F. 2022b, *ApJ*, 936, 69, doi: [10.3847/1538-4357/ac8544](https://doi.org/10.3847/1538-4357/ac8544)
- Miller, M. C., Lamb, F. K., Dittmann, A. J., et al. 2019, *Astrophys. J. Lett.*, 887, L24, doi: [10.3847/2041-8213/ab50c5](https://doi.org/10.3847/2041-8213/ab50c5)
- . 2021, *Astrophys. J. Lett.*, 918, L28, doi: [10.3847/2041-8213/ac089b](https://doi.org/10.3847/2041-8213/ac089b)
- Most, E. R., Weih, L. R., Rezzolla, L., & Schaffner-Bielich, J. 2018, *Phys. Rev. Lett.*, 120, 261103, doi: [10.1103/PhysRevLett.120.261103](https://doi.org/10.1103/PhysRevLett.120.261103)

- Nagakura, H., Hotokezaka, K., Sekiguchi, Y., Shibata, M., & Ioka, K. 2014, *Astrophys. J. Lett.*, 784, L28, doi: [10.1088/2041-8205/784/2/L28](https://doi.org/10.1088/2041-8205/784/2/L28)
- Nedora, V., Bernuzzi, S., Radice, D., et al. 2021, *ApJ*, 906, 98, doi: [10.3847/1538-4357/abc9be](https://doi.org/10.3847/1538-4357/abc9be)
- Nedora, V., Schianchi, F., Bernuzzi, S., et al. 2022, *Classical and Quantum Gravity*, 39, 015008, doi: [10.1088/1361-6382/ac35a8](https://doi.org/10.1088/1361-6382/ac35a8)
- Perego, A., Radice, D., & Bernuzzi, S. 2017, *Astrophys. J. Lett.*, 850, L37, doi: [10.3847/2041-8213/aa9ab9](https://doi.org/10.3847/2041-8213/aa9ab9)
- Pian, E., D’Avanzo, P., Benetti, S., et al. 2017, *Nature*, 551, 67, doi: [10.1038/nature24298](https://doi.org/10.1038/nature24298)
- Pozanenko, A. S., Barkov, M. V., Minaev, P. Y., et al. 2018, *ApJL*, 852, L30, doi: [10.3847/2041-8213/aaa2f6](https://doi.org/10.3847/2041-8213/aaa2f6)
- Qi, Y.-Q., Liu, T., Huang, B.-Q., Wei, Y.-F., & Bu, D.-F. 2022, *Astrophys. J.*, 925, 43, doi: [10.3847/1538-4357/ac3757](https://doi.org/10.3847/1538-4357/ac3757)
- Radice, D., Perego, A., Hotokezaka, K., et al. 2018a, *Astrophys. J.*, 869, 130, doi: [10.3847/1538-4357/aaf054](https://doi.org/10.3847/1538-4357/aaf054)
- Radice, D., Perego, A., Zappa, F., & Bernuzzi, S. 2018b, *Astrophys. J. Lett.*, 852, L29, doi: [10.3847/2041-8213/aaa402](https://doi.org/10.3847/2041-8213/aaa402)
- Ren, J., Lin, D.-B., Zhang, L.-L., et al. 2019, *Astrophys. J.*, 885, 60, doi: [10.3847/1538-4357/ab4188](https://doi.org/10.3847/1538-4357/ab4188)
- Riley, T. E., Watts, A. L., Bogdanov, S., et al. 2019a, *Astrophys. J. Lett.*, 887, L21, doi: [10.3847/2041-8213/ab481c](https://doi.org/10.3847/2041-8213/ab481c)
- . 2019b, A NICER View of PSR J0030+0451: Nested Samples for Millisecond Pulsar Parameter Estimation, v1.0.0, Zenodo, doi: [10.5281/zenodo.3386449](https://doi.org/10.5281/zenodo.3386449)
- Riley, T. E., Watts, A. L., Ray, P. S., et al. 2021a, *Astrophys. J. Lett.*, 918, L27, doi: [10.3847/2041-8213/ac0a81](https://doi.org/10.3847/2041-8213/ac0a81)
- . 2021b, A NICER View of the Massive Pulsar PSR J0740+6620 Informed by Radio Timing and XMM-Newton Spectroscopy: Nested Samples for Millisecond Pulsar Parameter Estimation, v1.0.0, Zenodo, doi: [10.5281/zenodo.4697625](https://doi.org/10.5281/zenodo.4697625)
- Romero-Shaw, I. M., Talbot, C., Biscoveanu, S., et al. 2020, *MNRAS*, 499, 3295, doi: [10.1093/mnras/staa2850](https://doi.org/10.1093/mnras/staa2850)
- Shappee, B. J., Simon, J. D., Drout, M. R., et al. 2017, *Science*, 358, 1574, doi: [10.1126/science.aag0186](https://doi.org/10.1126/science.aag0186)
- Shibata, M., & Hotokezaka, K. 2019, *Annual Review of Nuclear and Particle Science*, 69, 41, doi: [10.1146/annurev-nucl-101918-023625](https://doi.org/10.1146/annurev-nucl-101918-023625)
- Smartt, S. J., Chen, T. W., Jerkstrand, A., et al. 2017, *Nature*, 551, 75, doi: [10.1038/nature24303](https://doi.org/10.1038/nature24303)
- Sun, X., Miao, Z., Sun, B., & Li, A. 2022, arXiv e-prints, arXiv:2205.10631. <https://arxiv.org/abs/2205.10631>
- Tanaka, M., Kato, D., Gaigalas, G., & Kawaguchi, K. 2020, *MNRAS*, 496, 1369, doi: [10.1093/mnras/staa1576](https://doi.org/10.1093/mnras/staa1576)
- Tanvir, N. R., Levan, A. J., González-Fernández, C., et al. 2017, *ApJL*, 848, L27, doi: [10.3847/2041-8213/aa90b6](https://doi.org/10.3847/2041-8213/aa90b6)
- Troja, E., Piro, L., van Eerten, H., et al. 2017, *Nature*, 551, 71, doi: [10.1038/nature24290](https://doi.org/10.1038/nature24290)
- Utsumi, Y., Tanaka, M., Tominaga, N., et al. 2017, *PASJ*, 69, 101, doi: [10.1093/pasj/psx118](https://doi.org/10.1093/pasj/psx118)
- Valenti, S., Sand, D. J., Yang, S., et al. 2017, *ApJL*, 848, L24, doi: [10.3847/2041-8213/aa8edf](https://doi.org/10.3847/2041-8213/aa8edf)
- Villar, V. A., Guillochon, J., Berger, E., et al. 2017, *Astrophys. J. Letters*, 851, L21, doi: [10.3847/2041-8213/aa9c84](https://doi.org/10.3847/2041-8213/aa9c84)
- Yu, Y.-W., Liu, L.-D., & Dai, Z.-G. 2018, *Astrophys. J.*, 861, 114, doi: [10.3847/1538-4357/aac6e5](https://doi.org/10.3847/1538-4357/aac6e5)
- Zhang, Z., Feng, X.-B., & Chen, L.-W. 2021, *Chinese Physics C*, 45, 064104, doi: [10.1088/1674-1137/abf428](https://doi.org/10.1088/1674-1137/abf428)
- Zhu, Z.-Y., Li, A., Hu, J.-N., & Shen, H. 2019, *PhRvC*, 99, 025804, doi: [10.1103/PhysRevC.99.025804](https://doi.org/10.1103/PhysRevC.99.025804)
- Zhu, Z.-Y., Zhou, E.-P., & Li, A. 2018, *Astrophys. J.*, 862, 98, doi: [10.3847/1538-4357/aacc28](https://doi.org/10.3847/1538-4357/aacc28)